Erythrocyte deformation in a microfluidic cross-slot channel†

Yann Henon,[a] Gregory J. Sheard[b] and Andreas Fouras*[a]

Red blood cell (RBC) deformation is a dominant factor in the rheological properties of blood in vessels smaller than 300 micrometers. The extensional flow within a microfluidic cross-slot microchannel has been proposed as a mechanism for measuring the deformation of cells. Three-dimensional simulations of red blood cell deformation in a microfluidic cross-slot channel are presented. Simulations show that the entry position and angular orientation of cells have a significant effect on deformation, with greater deformation occurring when cells enter either near the center or close to the wall. Cells of varying stiffness are simulated to emulate the effect of pathological conditions like diabetes or malaria, and it is found that cross-slot devices can effectively differentiate between cells of varying elasticity. Necessary sample sizes to differentiate between populations of healthy and diseased cells to a statistically significant level using a Wilcoxon rank-sum test are estimated and are found to decrease with lower flow rates. The capacity of such a device to differentiate populations of healthy RBCs and malarial RBCs at statistically significant levels with sample sizes as low as fifty is demonstrated.

1   Introduction

Red blood cells (RBCs) undergo large deformation as they pass through vessels, especially when travelling through narrow capillaries with diameters as small as 3 micrometers. A normal human RBC is a biconcave discoid of 6–8 micrometer diameter and 2 micrometer thickness.[1] This shape results in RBCs having a surface area 40% greater than a sphere of equal volume, facilitating deformation at constant volume and improving oxygen transport. The RBC membrane deforms readily under the effect of shearing forces, but experiences very little area dilation.[2] This is due to the mechanical properties of the membrane, which is composed of a phospholipid bilayer supported by cytoskeletal proteins. The membrane surrounds a fluid cytoplasm[3] which has a viscosity five times greater than that of the surrounding blood plasma.

The normal hematocrit for human blood is around 45%,[4] and hence the deformable properties of RBCs are an important contributor to the hydrodynamic properties of whole blood.[5] In vessels whose diameter is less than 300 micrometers, significant non-Newtonian effects are observed, a property known as the Fahræus–Lindqvist effect.[6] Several diseases, including diabetes and malaria, have been shown to alter the flexibility and distensibility of erythrocytes.[7] The malaria parasite, which claims the lives of over 2 million people annually, uses the RBC as a site for maturation. This considerably affects the mechanical properties of the cell, which loses its ability to undergo significant deformation.[8,9] Increased rigidity of the RBC membrane has been associated with hypertension.[10] Studies also show an increase in red blood cell stiffness in diabetic patients.[11,12] It has been hypothesised that this RBC stiffening is the primary instigating factor in diabetic renal disease.[12]

A number of technologies have been developed to study the mechanics of RBCs, including micropipette aspiration,[13] optical tweezers[14] and magnetic cytometry.[15] The complimentary application of these technologies has made it possible to study cells undergoing a variety of stress states. The use of microfluidics expands this capability to mimic the complex stress states that result from normal biological flow in an environment that closely resembles the natural environment for cells. Microfluidic devices can create shear forces through the use of features such as constrictions[16] or mixing through the use of junctions.[17] A device employing bifurcations[18] demonstrated the capacity to sort populations of diseased and healthy red blood cells, achieving greater than 90% recovery for late stage infected red blood cells, with the advantage of the device being simple and passive. A microchannel which with a network of branches with dimensions and topology similar to real vasculature showed high sensitivity when measuring the filterability of erythrocytes stiffened with glutaraldehyde, displaying a very nearly linear response.[19] Another device used periodically spaced, triangle-shaped pillars to measure cell deformability of

[a]*Laboratory for Dynamic Imaging, Department of Mechanical and Aerospace Engineering, Monash University, Melbourne, Australia. E-mail: Andreas.Fouras@ monash.edu*

[b]*Department of Mechanical and Aerospace Engineering, Monash University, Melbourne, Australia*

† Electronic supplementary information (ESI) available: Details of the numerical implementation, boundary conditions, numerical validation and comparison to experimental results. See DOI: 10.1039/c4ra04229h

erythrocytes with good sensitivity, and was able to measure 10^3 to 10^4 before clogging occurs.[20] A microfluidic device was created to imitate the process of micropipette aspiration while significantly reducing the need for specialised equipment and human technical skill, and obtained results consistent with previous micropipette aspiration studies.[21] Another microfluidic device studied erythrocyte deformability by measuring the pressure required to deform through a funnel shaped construction,[22] and was clearly able to differentiate between healthy and malarial cells at various stages of infection. The use of viscoelastic fluids in microchannels can enable a range of behaviours not achievable in purely Newtonian fluids. A rectangular microchannel containing a viscoelastic fluid was used to separate rigid red blood cells from red blood cells of normal elasticity.[23] Additionally, the device can isolate white blood cells from diluted whole blood. Another device demonstrated that a microchannel containing a dilute DNA solution could focus a stream of rigid particles with very high efficiency (>99.5%) over a wide range of flow rates. A microfluidic cross-slot channel featuring an extensional flow at the intersection between four channels, with two opposite channels providing inflow, and the two perpendicular channels providing outflow, was first introduced for the study of polymer extensional hysteresis,[24] and has since been used to study polymer cells and beads,[25] as well as for study of free vortex formation.[26] A cross-slot device has been shown to have the capacity to phenotype cells with a high throughput.[27] Additional work has been performed on cross-slot devices to reduce the effect of sharp corners on the region of homogenous flow in the center.[28] Recently, simulations demonstrated the possibility for dynamic cell sorting to be achieved on a lab-on-a-chip device by integrating an active control system with a microfluidic cross-slot.[29] Due to the balance between inflow and outflow, an extensional flow is formed in the centre of the device, leading to extensional forces that are capable of stretching a sample such as a cell or a polymer. The magnitude of this deformation depends on the boundary conditions for the flow, the geometry of the device, the properties of the fluid in the device, and the properties of the cell.

Numerical simulations elucidate the physics underlying microfluidic phenomena, through the ability to give a complete description of all variables involved in the system. For example, simulations were performed to assess the relative magnitudes of viscous dissipation, diffusion, and convection as functions of channel geometry in a microfluidic channel.[30,31] Numerical simulations also greatly assist in assessing device capability,[30,32,33] especially before incurring the potentially high costs of manufacturing. A number of numerical techniques have been developed capable of simulating complex multiphase flows at the microscopic scale. Boundary integral methods can simulate Stokes flow (at the zero-Reynolds-number limit) with very high numerical efficiency as the equations need only be solved on the interface, and have been used to model capsule behavior in shear flows[34,35] as well as in simple extensional flows.[36,37] Other techniques include the use of boundary-fitted grids for each phase[38] and the arbitrary Lagrangian–Eulerian method, in which the grid follows the fluid.[39] The front-tracking

method, an extension of the immersed boundary method, which solves the fluid equations on a fixed Eulerian grid while tracking the interface using a moving Lagrangian grid represented by a set of marker points[40,41] can simulate flows at nonzero Reynolds numbers involving deformable particles in complex geometries. This is advantageous in simulating red blood cells as they can be modeled as viscous liquid drops surrounded by an infinitely thin elastic membrane, which enables the higher-viscosity cytoplasm within the cell to be captured (which for RBCs has a viscosity five times greater than that of the surrounding fluid). The front-tracking method solves a single set of equations for both the fluid internal to the cell and the surrounding fluid. This avoids the costly computations associated with creating a new mesh as the cell moves. The front-tracking method has been used extensively in simulating behavior of capsules and drops in various flows, including shear flows,[42] extensional flows,[43] oscillating extensional flows,[44] and migration in channel flow.[45] It has also been used to model aggregation of cells,[46,47] simulate micropipette aspiration,[48] and study red blood cell and platelet migration in ducts and channels.[49] It is well suited for the study of the cross-slot device, as this flow does not possess an analytical solution.

In this paper a numerical method for large deformation of red blood cells is presented, based on a finite-difference flow solver and the front-tracking method for deformable interfaces. Red blood cell migration and deformation is simulated in a microfluidic cross-slot device. Results are presented over a range of flow velocities, lateral cell injection positions, and cell stiffnesses. These results are combined with probabilistic simulations to reach an assessment of the device capabilites, in terms of the capability of such a device to measure cell deformation and differentiate between populations of healthy and diseased red blood cells is assessed. The combined numerical and statistical approach employed allows estimation of required sample sizes for statistically significant results over a range of Reynolds numbers and device configurations.

2 Methodology

This section describes the model used in the present study for fluid-cell mechanics and transport.

2.1 Fluid solver

The incompressible Navier–Stokes equations for a fluid of varying viscosity are given by:

$$\rho\left(\frac{\partial \mathbf{u}}{\partial t} + (\mathbf{u}\cdot\nabla)\mathbf{u}\right) = -\nabla p + \nabla\cdot\tau + \mathbf{F}, \tag{1}$$

$$\nabla\cdot\mathbf{u} = 0, \tag{2}$$

where $\mathbf{u}$ is the fluid velocity, p is the pressure, $\mathbf{F}$ is an external force, ρ is the density, μ is the viscosity of the fluid and τ is the viscous stress tensor given by

$$\tau = \mu(\nabla\mathbf{u} + (\nabla\mathbf{u})^{\mathrm{T}}). \tag{3}$$

the coefficient $\mu(\mathbf{x}, t)$ is the viscosity for the entire fluid field which varies depending on the position of the capsule: $\mu = \mu_C$, while $\mu = \mu_0$ for all points outside the capsule. As μ varies with the motion and deformation of the erythrocyte, $\mu(\mathbf{x}, t)$ needs to be updated after every time step through the use of an indicator function $I(\mathbf{x})$[50] where

$$\mu(\mathbf{x}) = \mu_0 + (\mu_C - \mu_0)I(\mathbf{x}). \qquad (4)$$

The indicator function is updated at the end of each iteration, by identifying which side of the interface each node appears. Such a simple approach is suitable when there does not exist a risk of error due to two interfaces being nearby, while minimising computational costs as only points sufficiently near the interface need to be updated. Inertial effects can be significant in microfluidic devices when velocities are high, and hence the inertial term of the Navier–Stokes equations is included.[32] The equations are discretized spatially using a three-dimensional, second-order finite difference scheme, and are integrated forward in time using a pressure-increment projection method.[51] Throughout this study, the density and viscosity of the surrounding fluid are given as 1050 kg m^{-3} and 1.0 mPa s respectively. The ratio of the viscosity of the cytoplasm to the surrounding fluid used is 5.

2.2 Immersed boundary method

In the immersed boundary method, the Navier–Stokes equations for the fluid are solved on a fixed Eulerian grid while the forces arising from deformation of the cell are computed on a moving front (Fig. 1a). A single set of equations are used for the entirety of the flow field, and allow variations in fluid density and viscosity.[52] The forces arising from cell deformation are accounted for in the fluid by introducing a body force $\mathbf{F}(\mathbf{x}, t)$:

$$\mathbf{F}(\mathbf{x}, t) = \int_{\partial S} f(\mathbf{x}', t)\delta(\mathbf{x} - \mathbf{x}')\mathrm{d}\mathbf{x}', \qquad (5)$$

where δ is the delta function, ∂S is the entire fluid domain, f is a force on the interface arising from membrane deformation, $\mathbf{x}$ is a point in the flow domain and $\mathbf{x}'$ is a point on the membrane. The use of a delta function δ accounts for the fact that forces are concentrated at the boundary. The thickness of a red blood cell membrane is around 2 nm, three orders of magnitude smaller that its overall diameter. As such, the use of a delta function is appropriate. However, points on the moving mesh of the cell generally do not coincide with those on the fixed Eulerian mesh of the fluid. Therefore a smooth representation of the delta function is used,[40]

$$d(r) = \begin{cases} \left(\dfrac{1}{4h}\right)\left(1 + \cos\left(\dfrac{\pi r}{2h}\right)\right), & |r| < 2h. \\ 0, & |r| \geq 2h. \end{cases} \qquad (6)$$

This function smooths the force over up to four grid points in each dimension, for a total of 64 points. Note that this smoothing imposes limits on the immersed boundary method as it is difficult to account for cells located very close to a
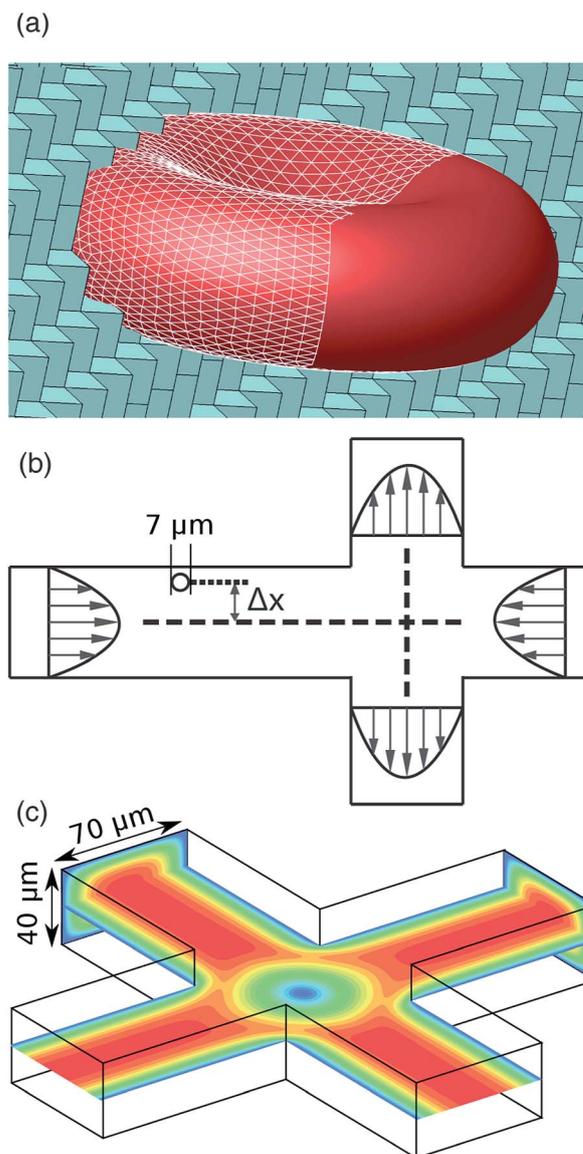

(a)

(b)

7 μm
Δx

(c)
70 μm
40 μm

Fig. 1 (a) A cutaway of the fixed Eulerian grid used to model the fluid, revealing the moving Lagrangian mesh discretizing a red blood cell in the implementation of the immersed boundary method. (b) Geometry of the cross-slot channel employed in these simulations. A blood cell enters the channel at a distance Δx from the channel centreline, and is deformed by the forces in the channel. One channel arm is longer so as to simulate cell migration as it enters the device. (c) Contour plot of velocity magnitude in the cross-slot channel. The flow is steady throughout, and an area of low velocity flow exists near the channel centre.

boundary. Other functions can be chosen, frequently with a narrower support to reduce the computational load. Once the fluid velocity is known, the points on the membrane can be advected by interpolating the velocity of the fluid using

$$\mathbf{u}(x') = \int_S \mathbf{u}(\mathbf{x})\delta(\mathbf{x} - \mathbf{x}')\mathrm{d}\mathbf{x}, \qquad (7)$$

where the same smooth representation of the delta function as was used previously is employed.

2.3 Cell modeling

The erythrocyte is represented as a three-dimensional capsule encased by an infinitesimally thin membrane which surrounds a fluid having a different viscosity than the surrounding fluid. Its shape is given by the Evans–Fung equation[53]

$$Z(R) = \pm 0.5 R_0 \left[1 - \left(\frac{R}{R_0} \right)^2 \right]^{\frac{1}{2}} \times \left[C_0 + C_1 \left(\frac{R}{R_0} \right)^2 + C_2 \left(\frac{R}{R_0} \right)^4 \right],$$

where $R_0 = 3.5\ \mu m$, $C_0 = 0.207161$, $C_1 = 2.002558$, $C_2 = -1.122762$ and $R^2 = X^2 + Y^2 \leq R_0^2$.

Several hyperelastic constitutive equations have been proposed to model red blood cell membranes. Frequently, a neo-Hookean model is used thanks to its simplicity.[46] The Yeoh strain energy function has been used to model blood cells deformed by optical tweezers, matching well with experimental results.[54] Here, a model developed to account for the specific properties of red blood cell membranes is used. Studies have shown that this membrane displays very high resistance to area dilation, a property which results from the lipid bilayer of the membrane, while the cytoskeleton provides a much smaller resistance to shear. These properties can be accounted for using the Evans and Skalak strain energy function, which is based on data from deformation measurements performed on red blood cells,[55]

$$W_{RBC} = K_{RBC} (\lambda_1 \lambda_2 - 1)^2 + \mu_{RBC} \left(\frac{\lambda_1^2 + \lambda_2^2}{2 \lambda_1^2 \lambda_2^2} - 1 \right), \qquad (8)$$

with $K_{RBC} = 500\ dyn\ cm^{-1}$ and $\mu_{RBC} = 0.006\ dyn\ cm^{-1}$. λ_1 and λ_2 are the principal planar stretches and the eigenvalues of the strain invariants $\mathbf{\Lambda}$. The strain invariants can be related to the surface deformation gradient tensor $\mathbf{A}$ through[56]

$$\mathbf{\Lambda}^2 = \mathbf{A} \cdot \mathbf{A}^T. \qquad (9)$$

The surface deformation gradient tensor is then defined as

$$\mathbf{A} = (\mathbf{I} - \mathbf{nn}) \cdot \mathbf{C} \cdot (\mathbf{I} - \bar{\mathbf{n}}\bar{\mathbf{n}}), \qquad (10)$$

where $\mathbf{C}$ is the deformation gradient tensor, $\bar{n}$ and n are the unit normal vector to the undeformed and deformed membranes, respectively.

$$\mathbf{C} = \frac{\partial \mathbf{X}}{\partial \bar{\mathbf{X}}}. \qquad (11)$$

$\mathbf{X}$ is the position of the points on the membrane in the deformed state, while $\bar{\mathbf{X}}$ is the position in the initial undeformed state. In the numerical implementation, the cell membrane is discretised into a mesh of six-node curved triangular elements and a standard procedure is followed.[35] The mesh is unstructured and created using icosahedral subdivision, avoiding the formation of poles which results from the use of a structured mesh on objects with the topology of a sphere.

A full validation has been performed to ensure the accuracy of the code. This was done by simulating a spherical capsule in an infinite shear flow and measuring the deformation at the steady-state for a variety of capillary numbers. Results from the current code are compared to predictions from small deformation at low capillary numbers,[56] and to results from immersed boundary and boundary integral simulations at larger capillary numbers. This validation test has the advantage of utilising all aspects of the solver. Results show that our simulations match closely with those produced using other techniques, and are especially similar to results from the immersed boundary method. Further details of the validation are available in the ESI.†

2.4 Problem set-up

Velocity Dirichlet boundary conditions for the channel inlets and outlets are imposed, where the velocity is given by the analytical solution for fully-developed viscous flow through a duct with square cross-section.[57] The full expression is available in the ESI.† Zero-velocity no-slip boundary conditions are imposed at the wall. The use of a staggered variable arrangement obviates the need to define boundary conditions for pressure at the walls.[58] The cell enters the channel at a sufficient distance from the boundaries for boundary effects to be absent. The channel has a diameter of 70 micrometers and a depth of 40 micrometers, realistic parameters using current common manufacturing techniques. The resolution of the channel arms is 119 × 68. The simulated channel is asymmetrical (Fig. 1b), having one arm longer than the others. This arm is used as the input for the cell, as the extra length of the arm allows the cell to adapt to the shear forces in the inlet arm before reaching the region of interest.

2.5 Dimensionless parameters

The maximum velocity at the channel centreline is U. The Reynolds number for the channel is defined as $Re_{ch} = (\rho U D)/\mu$, where ρ and μ are the density and viscosity of the surrounding fluid, respectively. The characteristic length is the hydraulic diameter $d_H = (2WH)/(W + H)$, where W and H are the width and height of the channel, respectively. Additionally, a Reynolds number for the cell is also defined, $Re_{RBC} = (\rho U a)/\mu$. When not specified, the cell Reynolds number, Re_{RBC}, is being used in this study, where a is the cell radius. The capillary number $Ca = (\mu U)/G$ is the ratio of viscous forces to the elastic force of the red blood cell membrane.

3 Results and discussion

A single cell is introduced in an undeformed state on the vertical centre-plane of the cross-slot, and horizontally offset from the centreline of the inlet channel by a distance Δx. The cell has an angular orientation θ about the x-axis and ϕ about the y-axis, which due to the azimuthal symmetry of the cell is sufficient to describe all possible cell orientations. The flow has been allowed to reach a steady state before the cell is introduced. The cell initially travels down the channel, where it undergoes deformation due to the shear forces in the fully developed channel flow and tends to migrate away from the channel wall under the action of transverse forces resulting from the asymmetry created by the wall.[45] The deformation D is

measured as the ratio of the length of the major axis to the length of the minor axis $D \equiv \frac{L_{\mathrm{major}}}{L_{\mathrm{minor}}}$, where L_{major} and L_{minor} are the length of the major and minor axis respectively. This deformation tends to be larger nearer the channel walls, following the increased shear rate towards the walls due to the no-slip condition. The deformation resulting from channel flow is small compared to deformation due to extensional forces in the cross-slot. When a model cell was injected precisely on the channel centreline ($\Delta x = 0$ μm), it would become forever trapped at the stagnation point at the centre of the channel intersection. To avoid this circumstance, data was only obtained for cell displacements down to $\Delta x = 0.1$ μm. Comparison with existing experimental results[61] are provided in the ESI.† The numerical simulations show good agreement with the experimental results, especially at low and moderate flow rates. The set-up differs somewhat from the set-up shown in the simulations presented in this section due to the use of a viscoelastic fluid and the rounded corners in the microchannel, but still show the capability of the numerical method employed.

3.1 Characterisation of cell deformation and migration

The deformation of red blood cells in the cross-slot device centre is one of the primary considerations for assessing the capabilities of such a device. Considering the time history of the deformation of the blood cells make its possible to broadly discern three deformation modes (Fig. 2) depending on cell entry position. In the first mode, cells travelling near the centreline deform very little while in the channel arm, as is expected from the low shear rates in channel flow (Fig. 2c) near the channel centre. Once these cells have approached the center of the device, they show a large deformation along their principal axis and remain nearly symmetrical about both their minor and major axes (Fig. 2d). The lack of symmetry results from exposure to shear forces while in the channel arm that has resulted in some deformation, and the non-uniformity of shear forces in the cross-slot centre. In the second mode, cells travelling away from both the centerline and the walls experience limited amounts of shear and exhibit only a small amount of deformation. The shear forces in the channel arm are greater than they are in the first mode resulting in greater deformation, but there exists a region of low shear located between the cross-slot device centre and the device corners. In the third mode, cells travelling near the wall show a moderate amount of deformation and adopt a highly unsymmetrical shape (Fig. 2e). This deformation is due to the shear from boundary effects rather than from the extensional field created by the cross-slot. Shear rates in the device are maximal in proximity to the walls. As red blood cells normally cluster towards the center of vessels creating a cell-free zone near the wall,[4] the occurrence of the third mode of deformation is rare, as most cells are located closer to the center. Additionally, cells travelling near a boundary will tend to migrate away under the action of transverse forces. Numerically, it is necessary to maintain a buffer zone between the cell and the wall for the immersed boundary to remain accurate, because forces resulting from cell
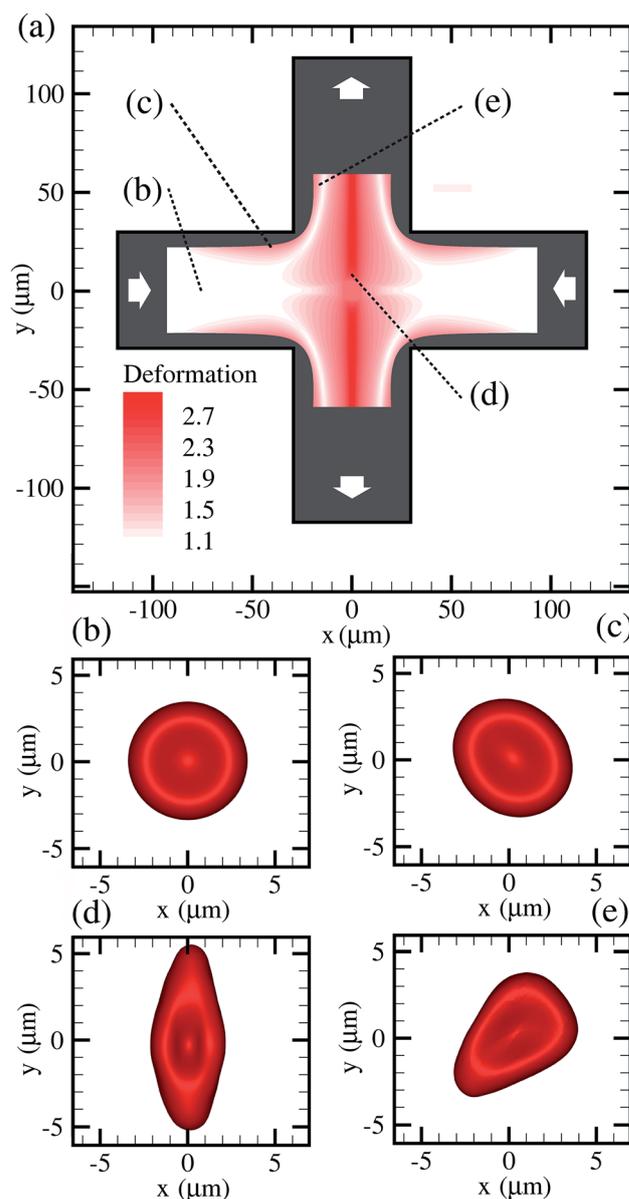

Fig. 2 (a) Contour map of cell deformation in the cross slot device at $\mathrm{Re_{RBC}} = 0.5$. Cells experience small to moderate deformation in the channel arms and potentially large deformations in the channel centre. (b) Undeformed biconcave discoid shape of an erythrocyte as it enters the channel. (c) Under the action of shear forces in the channel arm, cells undergo deformation and become asymmetrical with their major axis at a large angle to the flow. (d) Cells that enter near the device centre are stretched by mostly extensional forces and show the highest deformation. (e) Cells travelling far from the centreline enter the channel centre with already significant deformation, and are exposed to a complex combination of shear, extension and rotation.

deformation must be smoothed onto the surrounding area. The size of the buffer zone could be decreased by increasing the spatial resolution of the model, but there is limited interest in the study of cell behavior very near channel walls in these applications due to the presence of the cell-free zone.

Fig. 3a shows the magnitude of cell deformation in the cross-slot channel for Re = 0.5. Critically, cells further away from the
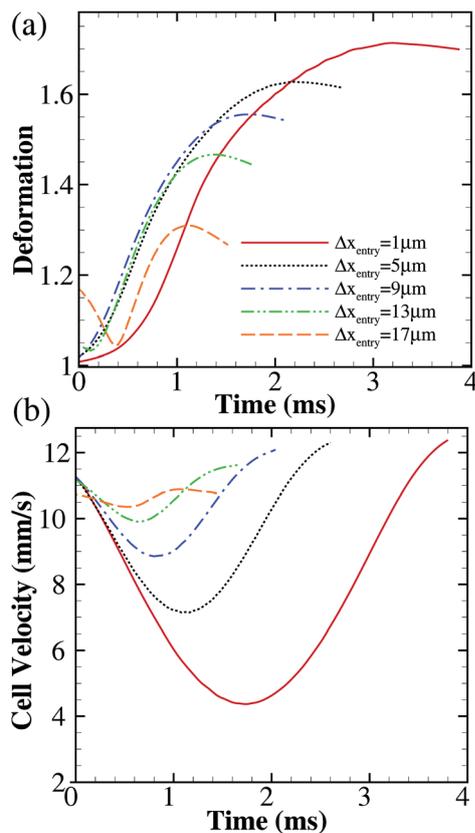
Fig. 3   Cell behaviour in the cross-slot device centre for Re = 0.05. (a) Time history of the magnitude of deformation D of cells with varying lateral displacement entry positions. Cells nearer the channel centreline exhibit more deformation and take longer to transit though the cross-slot centre. (b) Time history of cell velocity. Cells enter the channel centre with similar velocities, and cells nearer the centreline experience greater deceleration.

and then recovering as they move away. The longer transit time for cells nearer the channel centreline is due both to the necessity to travel a longer distance and to the fact that velocities are lower.

Increasing the velocity at which the fluid enters the channel leads to a higher Reynolds number and capillary number, resulting in higher deformation (Fig. 4), as similar cells are exposed to higher shear and extensional forces. Here D_{max} is the maximum deformation recorded over the transit of the cell through the central section of the cross-slot (Fig. 3a). The general trend is similar for all Reynolds numbers simulated, initially showing a decrease in cell deformation as distance from entry position increases, then reaching a minimum around $\Delta x = 17$ μm. Beyond that, maximum deformation increases again. The rate of change of the maximum deformation as a function of entry position decreases with decreasing Reynolds numbers.

channel centreline deform less. Although cells nearest the centreline deform most, their deformation as a function of time initially lags behind that of cells further away from the centre. This is due to differences in forces experienced by the cells as they travel through the cross-slot. In the device centre, cells experience a combination of shear forces and extensional forces which produce the complex deformation states that are observed. Hence cells nearer the channel centreline initially deform less as they experience only extensional forces, of magnitude comparable to the extensional forces experienced by cells further away from the channel centreline. There is a marked difference in time required for the cells to travel through the device centre, ranging from 1.77 ms for the cell starting at $\Delta x = 17$ μm to 3.81 ms for the cell starting at $\Delta x = 1$ μm. This may be advantageous from an experimental perspective, as cells experiencing more deformation remain in the device longer, possibly allowing more reliable and high-precision imaging. The cell entering at $\Delta x = 17$ μm has already significantly deformed as it enters the centre of the device, with $D = 1.16$, due to shear forces in the channel arm. For all cells, migration velocity shows a nearly parabolic profile (Fig. 3b), decreasing as cells approach the centre of the device
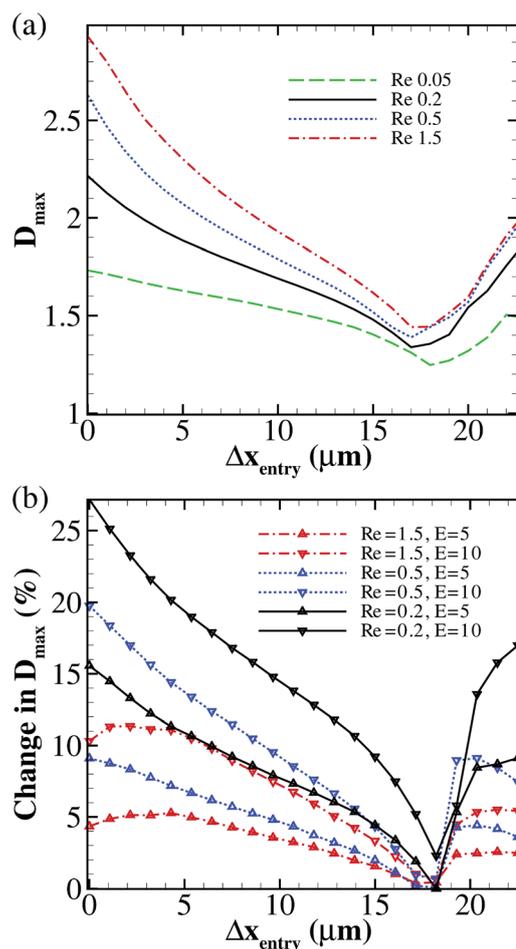

Fig. 4   (a) Maximum deformation state reached for cells entering the channel at different positions, shown here for Reynolds numbers 0.05, 0.2, 0.5 and 1.5. Greater Reynolds numbers lead to higher deformation of the cell for all entry positions. (b) Relative change of maximum cell deformation resulting from increased cell elasticity at Reynolds numbers 0.2, 0.5 and 1.5. Cell elasticity has been increased by a factor of 5 and 10 for $E = 5$ and $E = 10$ respectively. Greater Reynolds numbers result in smaller relative changes in maximum deformation.

3.2 Cell rotation

Cells entering the device are not fully characterised by their lateral displacement, as rotations around the x-axis and y-axis must also be considered to fully assess the abilities of such a device. Rotation around the z-axis has no effect due to the discoid shape of the undeformed cells. To fully study the behaviour of cells in a cross-slot device and estimate its capabilities, simulations are performed of cells with varying angle of rotation θ about the x-axis and ϕ about the y-axis, with θ and ϕ varying from $-\pi/2$ to $\pi/2$. Fig. 5 shows some results of the simulations for cells entering the channel at Re = 0.2. The deformation of the cell decreases when cells enter with a
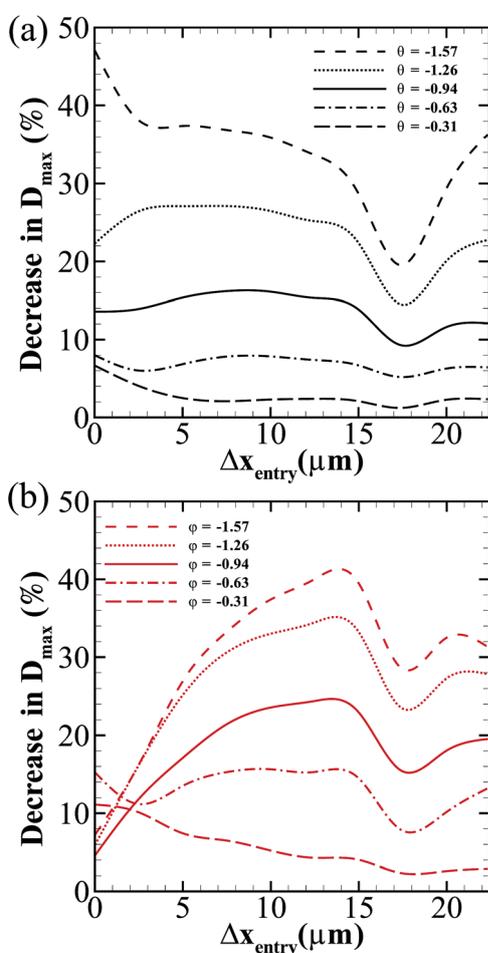

Fig. 5 (a) A plot of decrease in maximum cell deformation resulting from cell rotation about the x-axis at cell entry at Re = 0.2 for varying cell entry lateral positions compared to a cell entering with no rotation about the x-axis. For all angles and all lateral entry positions, the cells deform less when they enter with a rotation about the x-axis, and greater angles correspond to a greater decrease in maximum deformation (b) Decrease in maximum cell deformation resulting from cell rotation about the y-axis at cell entry at Re = 0.2 for varying cell entry lateral positions compared to a cell entering with no rotation about the y-axis. Similarly, for all angles and all lateral entry positions, the cells deform less when they enter with a rotation about the y-axis, and greater angles correspond to a greater decrease in maximum deformation. In this case, however, cells near the centreline show only a modest decrease in maximum deformation.

rotation about the x-axis and y-axis. The decrease in deformation of the cell depends on the inclination and the lateral position of entry. Results presented in Fig. 5 vary from $-\pi/2$ to 0, showing that the amount of deformation of the cells decreases at all lateral positions as the angle magnitude increases. This result is only violated for rotation about the y-axis when $\Delta x < \mu$m. Results from 0 to $\pi/2$ are not shown but nearly collapse with those presented: cell deformation strongly approximates symmetrical behaviour with respect to cell rotation.

3.3 Cell membrane elasticity

To achieve the goal of assessing the capability of a cross-slot microfluidic device, cells stiffened due to pathological conditions are simulated by increasing the elasticity modulus μ_{RBC}. The increase in stiffness associated with the malaria parasite *Plasmodium falciparum* depends on the stage of the infection (ring, trophozoite or schizont).[8,59] The measured elastic shear moduli using optical tweezers at various stages of *P. falciparum* infection are 16, 21.3 and 51.3 μN m^{-1} for ring, trophozoite and schizont stage, respectively. Using refractive index mapping, the measured shear moduli are 14.5, 35.0 and 71.8 μN m^{-1} for ring, trophozoite and schizont stage, respectively. The elastic shear modulus of the healthy red blood cell membrane is estimated to be around 6 μN m^{-1}. Here the ratio of the elasticity of an infected red blood cell to a healthy red blood cell is defined as E. Hence $E = 5$ and $E = 10$ are employed to simulate realistic values for trophozoite and schizont stages.

3.4 Assessment of cross-slot device capabilities

Based on the results presented in the previous section, it is possible to provide an assessment of the capability of a cross-slot microfluidic device to differentiate between populations of healthy and diseased RBCs. Many factors enter into the overall capability of such a device, including image resolution to measure cell deformation, frame rate to capture cell deformation, ability to keep cells sufficiently near the device centreline and sufficiently large sample sizes. As such, the necessary sample size to differentiate between healthy and diseased cells at a statistically significant level is estimated. Sample sizes from 10 to 1000 are employed, and 1000 estimations were performed for each sample size. These estimations are performed for Reynolds numbers 0.2, 0.5 and 1.5. The cells are assumed to enter the device with a deviation from the centreline Δx, where Δx is assumed to be normally distributed. The mean value of the distribution is $\mu = 0$, as deviation from the centreline can be either positive or negative, although the sign of the deviation has no impact. Three different distributions ranging from low to high are studied, corresponding to standard deviations $\sigma_{low} = 4$ μm, $\sigma_{medium} = 8$ μm and $\sigma_{high} = 12$ μm. As normal distributions are unbounded, some values for deviation would result in the cell being located either partly or wholly outside of the channel. In such cases, the value is discarded and replaced by a new value. Cells enter the channel with a rotation about the x-axis and y-axis, with a value chosen from the full range from $\pi/2$ to $\pi/2$, assuming a uniform distribution over the sphere.

Generally, microfluidic devices employ an input reservoir containing a dilute solution of red blood cells,[19] from which fluid and cells are drawn though the action of valves. As such, our simulations assume that the angle of the cells in the fluid has been randomised by the actions of drawing the blood, diluting it and placing it in the reservoir. Sheath flows have been shown to achieve hydrodynamic focusing resulting in cell distributions that resemble normal distributions.[60] More complex techniques have recently been introduced that can achieve significant focusing, such as the use of inertial forces[27] or the use of a viscoelastic fluid.[61] However, as we simulate the motion of the cell travelling down the device channel, the distribution of lateral displacements and rotation angles of the cells entering

the region of interest at the cross-slot device centre differs from the assumed distributions.

To account for noise and limited resolution in measurement, the deformations obtained from the simulations are combined with Gaussian white noise with standard deviation of $\sigma = 0.1$ μm. The measurements are then quantised to the imager resolution, 0.1 μm. For each sample, deformation measured by the simulated device for healthy cells and diseased cells ($E = 5$) are compared, and a Wilcoxon rank-sum test is performed to estimate if differences in measured deformation are statistically significant.[62] This test is appropriate as measurements are non-normally distributed. A significance level of 1% for rejecting the null hypothesis is employed. Results indicate that both Reynolds number and tightness of distribution of cell positions have a notable effect on sample size required (Fig. 6). In order to reach a p-value of 0.01, 292 samples are required at Re = 0.5 for σ_{high} while 67 samples are required for σ_{low} (Fig. 6a). This demonstrated the importance of focusing techniques in the design of microfluidic cross-slot devices. For σ_{medium}, a sample size of 57 is required at Re = 0.2 for a p-value of 0.01, while 271 samples are required at Re = 1.5 (Fig. 6b). The higher sample sizes at higher Reynolds numbers are mitigated by the fact that cells travel through the device faster due to the higher velocities, allowing more cell measurements in a given period of time. This demonstrates that cross-slot microfluidic devices have the capacity to distinguish between healthy and diseased red blood cell populations. Microfluidic devices can also be used for quantitative measurement of cell properties. Estimation of cell elasticity relies on repeated measurement of cell deformation in the cross-slot device centre. Accurate measurement then depends on consistent focusing of cells in the device centre, as deviations will lead to cells deforming less and hence underestimation of cell elasticity. Generally, it is convenient to consider a limited area of the device center as focused. If the
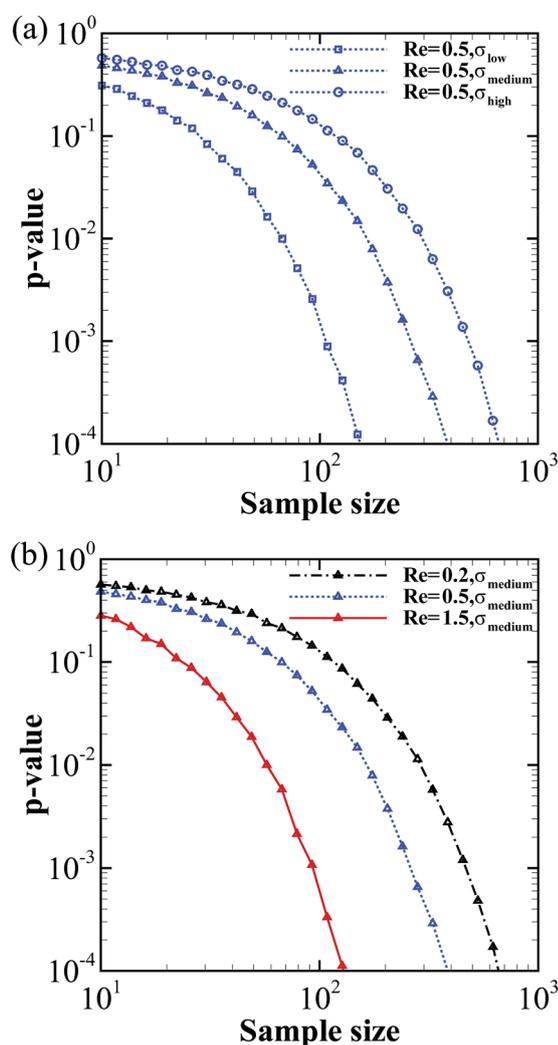

Fig. 6 Sample sizes needed to differentiate between healthy and diseased red blood cells using the cross-slot device at varying statistically significant levels, shown over a range of Reynolds numbers (a) and for different distributions in the position of cells entering the device (b). The cells enter the channel with a random position and orientation. Diseased cells have greater membrane elasticity and hence tend to deform less. Noisy measurements of cell length are made and used to identify healthy and diseased cell populations. Greater Reynolds numbers in the channel require larger cell sample sizes to achieve similar p-values as smaller Reynolds numbers.
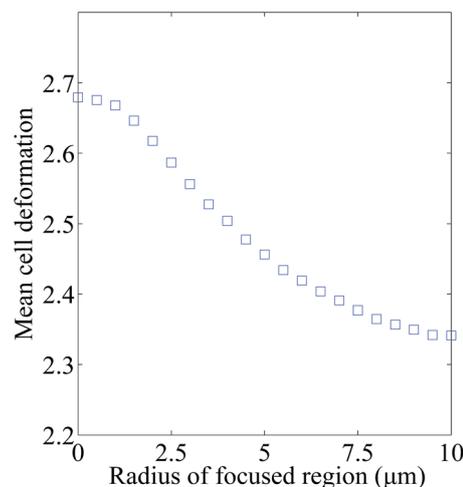

Fig. 7 Mean deformation of cells travelling through the cross-slot device center depending on the radius of the focused region. Cells lying outside of the focused area are ignored. Mean deformation decreases as radius of focusing area increases, demonstrating the importance of a small focus area.

area is too large, there is significant deviation in cell deformation. Conversely, if the area is too small, the device may be impractical as too many cells do not enter the area. In practice, the area that is practical depends on the focusing device employed. Fig. 7 shows the effect of the radius of the circular focused area on mean measured cell deformation for a cross-slot device at Re = 0.5. Results show that larger focus areas do lead to errors in measurement of cell elasticities. An area of radius 4.8 μm is needed for a drop in deformation of less than 10%.

4 Conclusion

Behavior of red blood cells in a microfluidic cross-slot channel has been investigated using numerical simulations based on the front-tracking immersed boundary method at non-zero Reynolds numbers. Such devices are increasingly being fabricated and used, and the current work has provided quantitative estimates of their ability to be useful in situations such as differentiating healthy and diseased red blood cells. It was found that cells that entered the device nearer the channel centreline tend to reach larger maximum deformations then those that entered further away, although the trend reverses when very near the wall. It was also found that higher Reynolds numbers were associated with higher deformation for all possible entry positions of the cell. Lower Reynolds numbers were associated with a larger relative drop in maximum deformation between healthy and diseased red blood cells, an important criterion when seeking to distinguish between populations of cells. However, the effect was not uniform across entry positions, and tended to be especially large when the cell enters near the channel centreline. For a distance away from the wall of approximately $\Delta x = 17$ μm, cell deformation is minimal and larger Reynolds numbers have little effect in further deforming the cell. Cells took on a variety of shapes depending on their entry position in the channel. When they entered near the centreline, deformation was mainly a large stretching along the major axis. Cells that entered further away from the centreline took on asymmetrical shapes due to shear in the channel arm, and their maximally deformed shape resulted from a combination of this deformation due to shear and extension from the device centre. Cells of varying membrane elasticities were also simulated as a means of modeling the effect of pathological conditions such as malaria. Higher elasticities resulted in less overall deformation as expected. Additionally, cells entering near the channel centreline also showed a larger relative drop in maximum deformation than those travelling away from the centreline. Based on these results, sample sizes necessary to differentiate between populations of healthy and diseased cells to a statistically significant level as a function of Reynolds number and of the distribution of cell entry positions were estimated.

Acknowledgements

References

1 M. Bessis and R. I. Weed, *Living blood cells and their ultrastructure*, Springer, 1973.
2 T. W. Secomb, R. Skalak, N. Özkaya and J. F. Gross, *J. Fluid Mech.*, 1986, **163**, 405.
3 T. Fischer, M. Stohr-Lissen and H. Schmid-Schonbein, *Science*, 1978, **202**, 894–896.
4 A. S. Popel and P. C. Johnson, *Annu. Rev. Fluid Mech.*, 2005, **37**, 43–69.
5 R. Carr, *J. Rheol.*, 1981, **25**, 67–82.
6 A. R. Pries, D. Neuhaus and P. Gaehtgens, *Am. J. Physiol.*, 1992, **263**, H1770–H1778.
7 R. A. Jamison, J. a. Armitage, J. Carberry, M. J. Kitchen, S. B. Hooper and A. Fouras, *Curr. Pharm. Biotechnol.*, 2012, **13**, 2128–2140.
8 F. K. Glenister, R. L. Coppel, A. F. Cowman, N. Mohandas and B. M. Cooke, *Blood*, 2002, **99**, 1060–1063.
9 Y. Park, M. Diez-Silva, G. Popescu, G. Lykotrafitis, W. Choi, M. S. Feld and S. Suresh, *Proc. Natl. Acad. Sci. U. S. A.*, 2008, **105**, 13730–13735.
10 H. G. Roggenkamp, F. Jung, H. P. Nüttgens, H. Kiesewetter, E. B. Ringelstein and R. Schneider, *Klin. Wochensch.*, 1986, **64**, 1091–1096.
11 N. Babu and M. Singh, *Clin. Hemorheol. Microcirc.*, 2004, **31**, 273–280.
12 M. Garnier, J. R. Attali, P. Valensi, E. Delatour-Hanss, F. Gaudey and D. Koutsouris, *Metabolism*, 1990, **39**, 794–798.
13 R. M. Hochmuth, *J. Biomech.*, 2000, **33**, 15–22.
14 M. Dao, C. Lim and S. Suresh, *J. Mech. Phys. Solids*, 2003, **51**, 2259–2280.
15 N. Wang and D. E. Ingber, *Biochem. Cell Biol.*, 1995, **73**, 327–335.
16 J. P. Arata and A. Alexeev, *Soft Matter*, 2009, **5**, 2721.
17 A. Neild, T. W. Ng, G. J. Sheard, M. Powers and S. Oberti, *Sens. Actuators, B*, 2010, **150**, 811–818.
18 H. W. Hou, A. A. S. Bhagat, A. G. L. Chong, P. Mao, K. S. W. Tan, J. Han and C. T. Lim, *Lab Chip*, 2010, **10**, 2605–2613.
19 S. S. Shevkoplyas, T. Yoshida, S. C. Gifford and M. W. Bitensky, *Lab Chip*, 2006, **6**, 914–920.
20 H. Bow, I. Pivkin, M. Diez-Silva and S. Goldfless, *Lab Chip*, 2011, **11**, 1065–1073.
21 Q. Guo, S. Park and H. Ma, *Lab Chip*, 2012, **12**, 2687–2695.
22 Q. Guo, S. J. Reiling, P. Rohrbach and H. Ma, *Lab Chip*, 2012, **12**, 1143–1150.
23 S. Yang, S. S. Lee, S. W. Ahn, K. Kang, W. Shim, G. Lee, K. Hyun and J. M. Kim, *Soft Matter*, 2012, **8**, 5011.

24 C. Schroeder, H. Babcock, E. Shaqfeh and S. Chu, *Science*, 2003, **301**, 1515–1519.

25 P. E. Arratia, C. C. Thomas, J. Diorio and J. P. Gollub, *Phys. Rev. Lett.*, 2006, **96**, 144502.

26 M. S. N. Oliveira, F. T. Pinho and M. A. Alves, *J. Fluid Mech.*, 2012, **711**, 171–191.

27 D. R. Gossett, H. T. K. Tse, S. a. Lee, Y. Ying, A. G. Lindgren, O. O. Yang, J. Rao, A. T. Clark and D. Di Carlo, *Proc. Natl. Acad. Sci. U. S. A.*, 2012, **109**, 7630–7635.

28 F. J. Galindo-Rosales, M. S. N. Oliveira and M. a. Alves, *RSC Adv.*, 2014, **4**, 7799.

29 M. D. Curtis, G. J. Sheard and A. Fouras, *Lab Chip*, 2011, **11**, 2343–2351.

30 D. A. Boy, F. Gibou and S. Pennathur, *Lab Chip*, 2008, **8**, 1424–1431.

31 J. Koo and C. Kleinstreuer, *J. Micromech. Microeng.*, 2003, **13**, 568–579.

32 D. Di Carlo, *Lab Chip*, 2009, **9**, 3038–3046.

33 V. Cristini and Y.-C. Tan, *Lab Chip*, 2004, **4**, 257–264.

34 C. Pozrikidis, *J. Fluid Mech.*, 1995, **297**, 123–152.

35 S. Ramanujan and C. Pozrikidis, *J. Fluid Mech.*, 1998, **361**, 117–143.

36 E. Lac, D. Barthès-Biesel, N. A. Pelekasis and J. Tsamopoulos, *J. Fluid Mech.*, 2004, **516**, 303–334.

37 S. Kwak and C. Pozrikidis, *Phys. Fluids*, 2001, **13**, 1234.

38 G. Ryskin and L. G. Leal, *J. Fluid Mech.*, 1984, **148**, 19–35.

39 H. Hu, *J. Comput. Phys.*, 2001, **169**, 427–462.

40 C. S. Peskin, *Acta Numerica*, 2003, **11**, 479–517.

41 G. Tryggvason, *J. Comput. Phys.*, 2001, **169**, 708–759.

42 D. Le, J. White, J. Peraire, K. Lim and B. Khoo, *J. Comput. Phys.*, 2009, **228**, 8427–8445.

43 X. Li and K. Sarkar, *J. Comput. Phys.*, 2008, **227**, 4998–5018.

44 X. Li and K. Sarkar, *Phys. Fluids*, 2005, **17**, 027103.

45 S. K. Doddi and P. Bagchi, *Int. J. Multiphase Flow*, 2008, **34**, 966–986.

46 P. Bagchi, P. C. Johnson and A. S. Popel, *J. Biomech. Eng.*, 2005, **127**, 1070–1080.

47 Y. Liu and W. Liu, *J. Comput. Phys.*, 2006, **220**, 139–154.

48 G. Agresar, J. Linderman, G. Tryggvason and K. Powell, *J. Comput. Phys.*, 1998, **143**, 346–380.

49 H. Zhao, E. S. G. Shaqfeh and V. Narsimhan, *Phys. Fluids*, 2012, **24**, 011902.

50 S. Unverdi and G. Tryggvason, *J. Comput. Phys.*, 1992, **100**, 25–37.

51 D. Brown, R. Cortez and M. Minion, *J. Comput. Phys.*, 2001, **168**, 464–499.

52 R. Scardovelli and S. Zaleski, *Annu. Rev. Fluid Mech.*, 1999, **31**, 567–603.

53 E. Evans and Y. C. Fung, *Microvasc. Res.*, 1972, **4**, 335–347.

54 C. Chee, H. Lee and C. Lu, *Phys. Lett. A*, 2008, **372**, 1357–1362.

55 R. Skalak and A. Tozeren, *J. Biomech.*, 1973, **43**, 2753–2764.

56 D. Barthès-Biesel and J. M. Rallison, *J. Fluid Mech.*, 1981, **113**, 251.

57 S. Kuriakose and P. Dimitrakopoulos, *Phys. Rev. E: Stat., Nonlinear, Soft Matter Phys.*, 2011, **84**, 1–22.

58 J. Kim and P. Moin, *J. Comput. Phys.*, 1985, **59**, 308–323.

59 S. Suresh, J. Spatz, J. P. Mills, A. Micoulet, M. Dao, C. T. Lim, M. Beil and T. Seufferlein, *Acta Biomater.*, 2005, **1**, 15–30.

60 Y.-J. Chiu, S. H. Cho, Z. Mei, V. Lien, T.-F. Wu and Y.-H. Lo, *Lab Chip*, 2013, **13**, 1803–1809.

61 S. Cha, T. Shin, S. S. Lee, W. Shim, G. Lee, S. J. Lee, Y. Kim and J. M. Kim, *Anal. Chem.*, 2012, **84**, 10471–10477.

62 J. D. Gibbons, *Nonparametric Statistical Inference*, Marcel Dekker, 1985.